

Cellular/Dendritic Transition and Microstructure Evolution during Transient Directional Solidification of Pb-Sb Alloys

DANIEL M. ROSA, JOSÉ E. SPINELLI, IVALDO L. FERREIRA, and AMAURI GARCIA

Recent studies of lead-antimony alloys, used for the production of positive electrodes of lead-acid batteries, have assessed the influences of both the microstructural morphology and of solute redistribution on the surface corrosion resistance in sulfuric acid solution, and have shown that cellular structures and dendritic structures have different responses on the corrosion rate of such alloys. The present article focuses on the search of adequate solidification conditions (alloy composition, cooling rate, and solidification velocity), which determine the occurrence of a microstructural transition from the cellular to the dendritic regime during the transient unidirectional solidification of hypoeutectic Pb-Sb alloys and on the microstructural evolution after such transition. The experimental data refers to the solidification of four hypoeutectic Pb-Sb alloys (2.2, 2.5, 3, and 6.6 wt pct Sb) and of the eutectic composition. The experimental results include transient metal/mold heat-transfer coefficients, liquidus isotherm velocity, cooling rate, and cellular and dendritic spacings. It was found that the cooling rate dependence on cellular and primary dendritic spacings is characterized by an experimental law of the form $\lambda_1 = A \cdot \dot{T}^{-0.55}$, which seems to be independent of composition where $A = 60$ represents the alloys undergoing a cellular growth and $A = 115$ can describe the dendritic growth. The sudden change on such multiplier has occurred for the Pb 2.2 wt pct Sb alloy, *i.e.*, for the cellular/dendritic transition.

DOI: 10.1007/s11661-008-9542-1

© The Minerals, Metals & Materials Society and ASM International 2008

I. INTRODUCTION

SINCE the early 1980s, a number of metallurgists, physicists, and mathematicians have investigated the solid/liquid interface morphologies during solidification in which the cellular/dendritic growth is one of the most complicated structural patterns and is also the most prevalent form of crystallization.^[1-7] The cellular and dendritic spacings are important microstructural parameters resulting from the solidification process, because it is well known that these spacings exercise a significant influence on the properties of castings. They affect the microscopic segregation existing between the cellular or dendritic ramifications, and consequently, the mechanical behavior. Some recent studies have pointed out the effect of microstructure and particularly of dendrite spacings on mechanical properties of as-cast alloys.^[8-10] It has also been recently reported in the literature that the microstructural morphologies have a strong influence on the corrosion resistance of binary alloys. The cooling rate imposed during solidification affects cellular and dendritic spacings, and the solute redistribution, which connected with the electrochemical behavior of

solute and solvent will affect the resulting corrosion resistance.^[5,10-14]

The correct determination of thermal parameters such as the temperature gradient (G_L), solidification velocity (V_L), and cooling rate (\dot{T}) acting during solidification is very important, because the growth of regular cells occurs in low growth rate conditions, is perpendicular to the solid/liquid interface, in the direction of heat flow extraction, and practically independent of the crystallographic orientation. If G_L is reduced and V_L increased, the region constitutionally supercooled is extended and the cells begin to change their behavior to configuration of the malt cross type, and the crystallographic direction starts to exercise a strong effect. With the gradual increase of V_L , the cells begin to present side perturbations that are denominated ramifications or secondary arms defining the dendritic structure.^[1,15,16]

During unidirectional growth under steady-state conditions, G_L and V_L are independently controlled and held constant with time, while in the non-steady-state regime, the temperature gradient and growth rate vary freely in time. It is well known that the solidification microstructure of a single phase alloy undergoes a transition from a cellular to dendritic interface as the velocity increases. Figure 1 shows a schematic representation of such influence on microstructure formation. Further increase in the solidification velocity changes the interface morphology from dendritic back to cellular and finally planar.^[17,18]

Lee and co-authors^[18] carried out directional solidification experiments using 18Cr ferritic stainless steels with 0, 3, and 5 wt pct Al under steady-state heat flow

DANIEL M. ROSA, Postdoctoral Fellow, is with the Faculty of Technology, University of Brasilia, 70910-90, Brasilia, DF, Brazil. JOSÉ E. SPINELLI and IVALDO L. FERREIRA, Postdoctoral Fellows, and AMAURI GARCIA, Professor, are with the Department of Materials Engineering, State University of Campinas, UNICAMP, 13083-970 Campinas, SP, Brazil. Contact e-mail: amaurig@fem.unicamp.br

Manuscript submitted November 22, 2007.

Article published online May 7, 2008

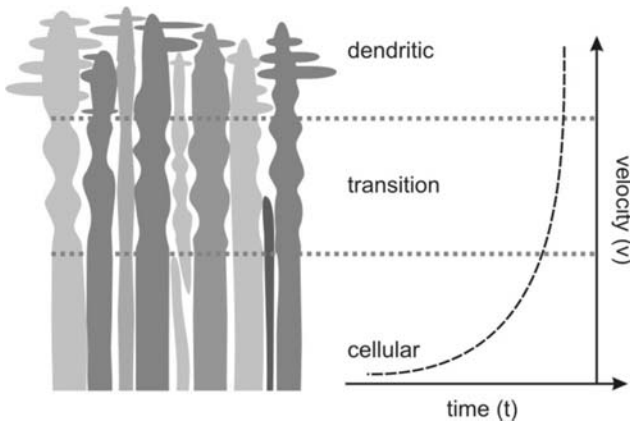


Fig. 1—Influence of solidification velocity on microstructure formation during vertical solidification.

conditions to study the high-velocity dendrite to cellular transition. They have observed that the primary dendrite arm spacing is higher than cellular spacings for both low- and high-velocity regimes, and the transition conditions are discussed by using the tip temperature vs velocity for cellular and dendritic morphologies.

Most of the unidirectional solidification studies existing in literature have been carried out with a view of characterizing the cellular/dendritic transition involving solidification in steady-state heat flow conditions. On the other hand, the analysis of these structures in the non-steady-state regime is scarce in the literature, despite its importance, since it encompasses the majority of industrial solidification processes. Rocha *et al.*^[19] have studied the cellular to dendritic transition during the transient directional solidification of Sn-Pb hypoeutectic alloys. They have found that such transition can be observed in the range of compositions between 2 and 3 wt pct Pb. The Sn 2.5 wt Pb alloy casting has been entirely characterized by a transition microstructure observed along a range of cooling rates from 0.5 to 5.2 K/s.

Lead-antimony alloys are widely used for the production of superior grids of positive electrodes of lead-acid batteries (1 to 5 wt pct Sb). These alloys are relatively strong and creep resistant and can be cast into rigid dimensionally-stable grids, which are capable of resisting the stresses of the charge-discharge reactions.^[20,21] The antimony content of a Pb-Sb alloy affects the microstructural pattern, mechanical properties, and electrochemical behavior of active materials and corrosion layers on the electrode. Recent studies of lead-antimony alloys assessing the influences of both the microstructural morphology and of solute redistribution on the surface corrosion resistance in sulfuric acid solution have shown that cellular structures and dendritic structures have different responses on the corrosion rate of such alloys.^[13,14] Coarse cells tend to yield higher corrosion resistance, while finer dendritic arrangements have superior corrosion response.

The present article focuses on the search of adequate solidification conditions (alloy composition, cooling rate, and solidification velocity), which determine the

occurrence of a microstructural transition from the cellular to the dendritic regime during the transient unidirectional solidification of hypoeutectic Pb-Sb alloys, and on the microstructural evolution after such transition. The experimental data refers to the solidification of four hypoeutectic Pb-Sb alloys (2.2, 2.5, 3, and 6.6 wt pct Sb) and of the eutectic composition. The experimental results include transient metal/mold heat-transfer coefficients, liquidus isotherm velocity, cooling rate, and cellular and dendritic spacings. In order to assess the application of the existing predictive dendritic growth models under non-steady-state freezing, the experimental dendritic spacings were compared with the corresponding theoretical predictions.

II. DENDRITIC SPACING MODELS

Among the theoretical models existing in the literature, only those proposed by Hunt and Lu^[22] for primary spacings and Bouchard-Kirkaldy^[23] for primary and secondary spacings encompass solidification in non-steady-state heat flow conditions. Hunt,^[24] Kurz and Fisher,^[25,26] and Trivedi^[27] have derived primary spacing formulas, which apply for steady-state conditions. The theoretical models for determination of dendritic spacings proposed by these authors are shown in Eqs. [1] through [8]:

$$\lambda_1 = 2.83[\Gamma m_L C_0(1 - k_0)D]^{1/4} G_L^{-1/2} V_L^{-1/4} \quad \text{(Hunt, cellular/dendritic)} \quad [1]$$

$$\lambda_1 = 4.3 \left(\frac{\Gamma \Delta T D}{k_0} \right)^{1/4} G_L^{-1/2} V_L^{-1/4} \quad \text{(Kurz and Fisher, cellular/dendritic)} \quad [2]$$

$$\lambda_1 = 2.83[L_T \Gamma m_L C_0(1 - k_0)D]^{1/4} G_L^{-1/2} V_L^{-1/4} \quad \text{(Trivedi, dendritic)} \quad [3]$$

$$\lambda'_1 = 0.07798 V'^{(a-0.75)} (V' - G')^{0.75} G'^{-0.6028} \quad \text{(Hunt-Lu, dendritic)} \quad [4]$$

where

$$a = -1.131 - 0.1555 \log_{10}(G') - 0.007589 [\log_{10}(G')]^2 \quad [5]$$

$$\lambda'_1 = \frac{\lambda_1 \Delta T}{\Gamma k_0}, \quad G' = \frac{G_L \Gamma k_0}{\Delta T^2}, \quad \text{and} \quad V' = \frac{V_L \Gamma k_0}{D \Delta T} \quad [6]$$

$$\lambda_1 = a_1 \left(\frac{16 C_0^{1/2} G_0 \epsilon \Gamma D}{(1 - k_0) m_L G_L V_L} \right)^{1/2} \quad \text{(Bouchard-Kirkaldy, primary dendritic)} \quad [7]$$

where λ_1 is the primary dendritic spacing, Γ is the Gibbs–Thomson coefficient, m_L is the liquidus line slope, k_0 the solute partition coefficient, C_0 is the alloy composition, D is the liquid solute diffusivity, ΔT is the difference between the liquidus and solidus equilibrium temperatures, V_L is the dendrite tip growth rate, G_L is the temperature gradient in front of the liquidus isotherm, $G_0\epsilon$ is a characteristic parameter $\approx 600 \times 6 \text{ K cm}^{-1}$,^[23] and a_1 is the primary dendrite-calibrating factor. The spacings proposed by the Hunt–Lu model (Eqs. [4] through [6]) refer to the radius rather than to the more commonly measured diameter, and they are minimum spacings; thus, the calculated values need to be multiplied by 2 to 4 for comparison with measured spacings.

The Trivedi model^[27] is a result of a Hunt’s model modification, where L_T is a constant that depends on harmonic perturbations. According to Trivedi, for dendritic growth, L is equal to 28.

For secondary dendrite spacings, Bouchard and Kirkaldy^[23] derived an expression, which is very similar to the Mullins and the Sekerka temperature gradient independent marginal wavelength formula, which is given by

$$\lambda_2 = 2\pi a_2 \left(\frac{4\Gamma}{C_0(1-k_0)^2 T_F} \left(\frac{D}{V_L} \right)^2 \right)^{1/3} \quad [8]$$

where a_2 is the secondary dendrite-calibrating factor, which depends on the alloy composition, and T_F is the fusion temperature of the solvent.

Feurer and Wunderlin^[28] and Kirkwood^[29] have derived secondary spacing formulas as a function of local solidification time, which differ only by a small factor in the numerical constant, and can be expressed as

$$\lambda_2 = K(Mt_{SL})^{1/3} \text{ (m)} \quad [9]$$

where

$$M = -\frac{\Gamma D}{(1-k_0)m_L(C_E - C_0)} \ln \left(\frac{C_E}{C_0} \right) \text{ (m}^3/\text{s)} \quad [10]$$

$K = 5.5$ (Feurer and Wunderlin) or $K = 5.0$ (Kirkwood), and C_E is the eutectic composition.

III. EXPERIMENTAL PROCEDURE

Experiments were carried out with Pb-Sb alloys (2.2, 2.5, 3.0, 6.6, and 11.2 wt pct Sb) with superheats of 10 pct above the liquidus temperature. The alloys were prepared with commercially pure metals, with chemical compositions shown in Table I. To prepare such alloys, proportional amounts of tin and antimony were first weighted by an analytical balance. Second, the materials were put into a silicon carbide crucible, heated, melted, and mixed. Finally, the cooling curves were obtained by imposing low cooling conditions and the typical experimental transformation temperatures (liquidus and eutectic) were compared to those of the equilibrium

Table I. Chemical Composition of Metals Used to Prepare the Pb-Sb Alloys

Metal	Chemical Composition (Wt Pct)						
	Pb	Sb	Fe	Si	Na	Cu	S
Sb	0.247	99.33	0.053	0.017	0.298	0.030	0.022
Pb	99.87	*	0.051	0.080	*	*	*

*Less than 50 ppm.

Pb-Sb phase diagram. In a second step, the alloy compositions were checked by X-ray fluorescence spectrometry. If necessary, further corrections of one of the elements were done until the desired composition was attained. The thermophysical properties of these alloys are summarized in Table II.

The solidification setup used in the experiments is detailed in Figure 2. It was designed in such way that the heat was extracted only through the water-cooled bottom, promoting vertical upward directional solidification. The stainless steel mold had an internal diameter of 50 mm, height 110 mm, and a wall thickness of 3 mm. To minimize radial heat losses, a solution of alumina in water has been applied to the inner surface of mold side walls by using a spray gun. After dried such layer of insulating alumina was about 500- μm thick. The bottom part of the mold was closed with a thin (3-mm thick) stainless steel sheet, which physically separates the metal from the cooling fluid.

The alloys were melted *in situ* and the lateral electric heaters had their power controlled in order to permit a desired melt superheat to be achieved. To start solidification, the electric heaters were disconnected, and at the same time the controlled water flow was initiated. The inlet water temperature was about 22 °C and the thermal readings have shown that such temperature was constant during the experiments. A rotameter was used to control water flow, which was kept constant about 11.5 L/min during each experiment. The device can promote water flow ranging between 4 and 30 L/min. The thermal acquisition system, which is composed of a data logger and a data reading software, was run from the signals of type J thermocouples. All thermocouples were calibrated considering the melting temperature of lead, exhibiting fluctuations of about 0.4 °C. Six thermocouples, sheathed in 1.6-mm outside diameter stainless steel protection tubes, were placed close to the central part of the cylindrical ingot and temperature was monitored during solidification at 5, 10, 15, 30, 50, and 70 mm from the heat extracting surface. The thermal readings were collected through an acquisition rate of two measurements per second.

The thermocouple readings were used to generate a plot of position from the metal/mold interface as a function of time corresponding to the liquidus front passing by each thermocouple. A curve fitting technique on these experimental points yielded a power function of position as a function of time. The derivative of this function with respect to time gave values for the liquidus

Table II. Thermophysical Properties of Alloys used in the Experimental Analysis*

Properties	Symbol	Pb	Sb	Pb 2.2 Pct Sb	Pb 2.5 Pct Sb	Pb 3 Pct Sb	Pb 6.6 Pct Sb	Pb 11.2 Wt Pct Sb
Thermal conductivity ($\text{W}\cdot\text{m}^{-1}\cdot\text{K}^{-1}$)	K_S	33.0	23.8	32.8	32.8	32.7	32.4	32.0
	K_L	29.7	19.7	29.5	29.4	29.4	29.0	28.6
Specific heat ($\text{J}\cdot\text{kg}^{-1}\cdot\text{K}^{-1}$)	c_S	129.8	209.0	131.5	131.8	132.2	135.1	138.7
	c_L	138.2	239.0	140.4	140.7	141.2	144.9	149.5
Density ($\text{kg}\cdot\text{m}^{-3}$)	ρ_S	11,340	6680	11,238	11,224	11,200	11,032	10,818
	ρ_L	10,678	6483	10,586	10,573	10,552	10,401	10,208
Latent heat of fusion ($\text{J}\cdot\text{kg}^{-1}$)	ΔH	26,205	163,000	29,215	29,625	30,309	35,234	41,526
Solute diffusivity ($\text{m}^2\cdot\text{s}^{-1}$)	D	—	—	3.0×10^{-9}	3.0×10^{-9}	3.0×10^{-9}	3.0×10^{-9}	3.0×10^{-9}
Gibbs–Thomson coefficient ($\text{m}\cdot\text{K}$)	Γ	—	—	9.89×10^{-8}	9.89×10^{-8}	9.89×10^{-8}	9.89×10^{-8}	9.89×10^{-8}
Liquidus temperature ($^\circ\text{C}$)	T_L	—	—	313.0	312.0	306.5	289	251.7
Solidus temperature (equilibrium) ($^\circ\text{C}$)	T_S	—	—	289.0	287.0	266.2	251.7	251.7
Eutectic temperature ($^\circ\text{C}$)	T_E	—	—	251.7	251.7	251.7	251.7	251.7
Liquidus slope ($^\circ\text{C}/\text{wt pct}$)	m_L	—	—	6.696	6.696	6.696	6.696	6.696
Partition coefficient	k_0	—	—	0.3125	0.3125	0.3125	0.3125	0.3125

*Sources: Ref. 5 and Thermo-Calc.

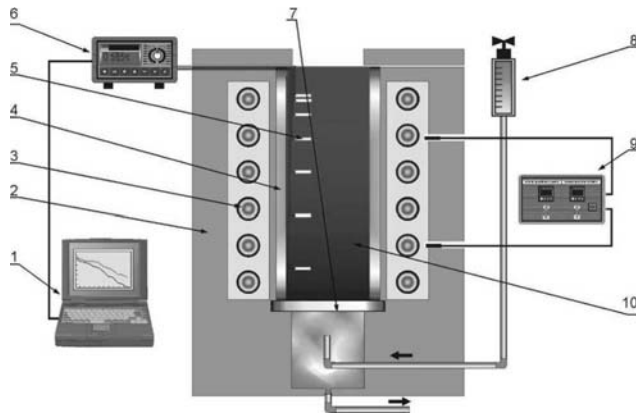


Fig. 2—Schematic representation of the experimental solidification setup: (1) computer and data acquisition software, (2) insulating ceramic shielding, (3) electric heaters, (4) mold, (5) thermocouples, (6) data logger, (7) heat-extracting bottom, (8) water flow meter, (9) temperature controller, and (10) casting.

isotherm velocity. Moreover, the data acquisition system employed permits accurate determination of the slope of the experimental cooling curves. Hence, the tip cooling rate was determined by considering the thermal data recorded immediately after the passing of the liquidus front by each thermocouple.

The cylindrical ingot was sectioned on a midplane, ground, polished, and etched with a solution to reveal the macrostructure. Two etching solutions were used: solution A (80 mL of nitric acid and 220 mL of distilled water); and solution B (45 g of $(\text{NH}_4)_2\text{MoO}_4$ dissolved in distilled water). Equal quantities of such solutions were mixed, with the samples being immersed in the resulting mixture at room temperature until the desired contrast was attained. A solution of ethylene diamine tetra-acetic acid (EDTA) was also used for removing the oxide formed at the surface.

Transverse (perpendicular to the growth direction) and longitudinal sections from the directionally

solidified specimen at six different positions along the ingot length were polished and etched with a solution (37.5 mL of glacial acetic acid and 15 mL of H_2O_2 , at 25°C) for microscopy examination. Image processing systems Neophot 32 (Carl Zeiss, Esslingen, Germany) and Leica Quantimet 500 MC (Leica Imaging Systems Ltd., Cambridge, England) were used to measure the cellular (λ_c) and dendrite spacings (λ_1 is primary dendritic arm spacing and λ_2 is secondary dendritic arm spacing). Thirty independent readings were done for each selected position, with the average taken to be the local spacing. The method used for measuring λ_c and λ_1 on the transverse section of each sample was the triangle method.^[30] The secondary dendrite arm spacing was measured on the longitudinal section by averaging the distance between adjacent side branches.

IV. RESULTS AND DISCUSSION

In cooled molds, the overall interfacial heat flow can be defined by a series of thermal resistances. The interfacial thermal resistance between the casting and the cooled steel sheet at the mold bottom ($1/h_{m/m}$) is generally the largest and the overall thermal resistance ($1/h_i$) is given by

$$\frac{1}{h_i} = \frac{1}{h_{m/m}} + \frac{e_S}{K_S} + \frac{1}{h_w} \quad [11]$$

where h_i is the overall heat-transfer coefficient between the casting surface and the cooling fluid, $h_{m/m}$ the heat-transfer coefficient between the casting surface and the steel surface at the bottom of the crucible, e_S the thickness of the stainless steel sheet that separates the metal from the cooling fluid, K_S its thermal conductivity, and h_w is the mold-coolant heat-transfer coefficient.

The results of experimental thermal analysis in castings were compared with simulations provided by a finite difference heat flow program, and an automatic

search has selected the best theoretical-experimental fit from a range of transient heat-transfer coefficient profiles, as described in a previous article.^[31] Figure 3(a) shows typical cooling curves obtained from four thermocouples inside the Pb-3 wt pct Sb alloy casting during the evolution of the directional solidification. Also seen are the best-fit numerical profiles referring to the four thermocouples, which are closer to the heat extracting surface.

Figure 3(b) shows the time dependence of the metal/coolant interface heat-transfer coefficient (h_i) during the course of different experiments of upward directional solidification of Pb-Sb alloys, including the profile obtained for the eutectic composition analysis. In order to permit more accurate values of h_i to be determined, a quadratic function has been used to characterize the initial melt profile, as discussed in a recent article.^[32] The thermophysical properties, the solidification range, and the melt fluidity are some of the factors affecting h_i . The surface roughness of the stainless steel sheet that separates the metal from the cooling fluid has been parameterized.

Although a single exponent (0.11) has been found for the power laws characterizing the variation of h_i with

time, different multipliers have been obtained. Such multipliers seem to be mainly linked to the wettability of the liquid layer in contact with the mold inner surface, *i.e.*, connected with the molten alloy fluidity. Both liquid metal and mold characteristics are involved in determining fluidity.^[33,34] Figure 3(c) shows the fluidity superimposed to the Pb-Sb phase diagram. The fluidity of Pb-Sb alloys decreases from pure lead up to a range of compositions between 3.5 and 8.0 wt pct Sb increasing again with increasing Sb content toward the eutectic composition. The two extremes of the composition range experimentally examined, *i.e.*, the Pb 2.2 wt pct Sb alloy and the eutectic composition are associated with the higher h_i profiles as shown in Figures 3(b) and (c). By observing Figures 3(c) and (d), a correlation between the multiplier (A) of the experimentally determined $h_i = f(t)$ equations and the fluidity values can be established.

The experimental thermal readings furnished by the six thermocouples do not provide a complete description of solidification thermal variables along the entire casting length. It would be convenient to have a numerical tool which could provide such thermal variables such as the liquidus isotherm velocity,

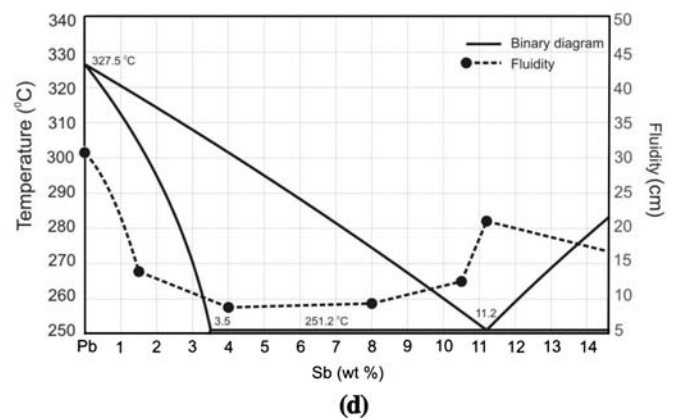
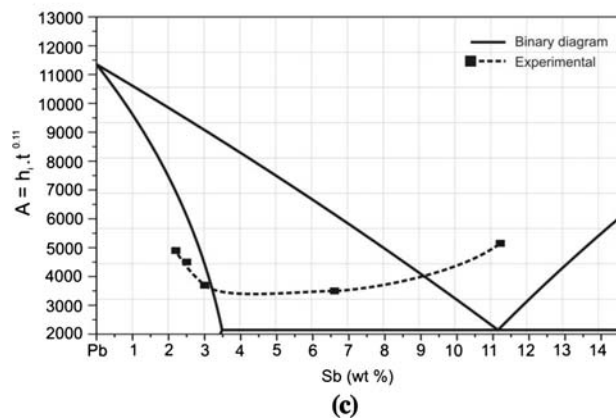
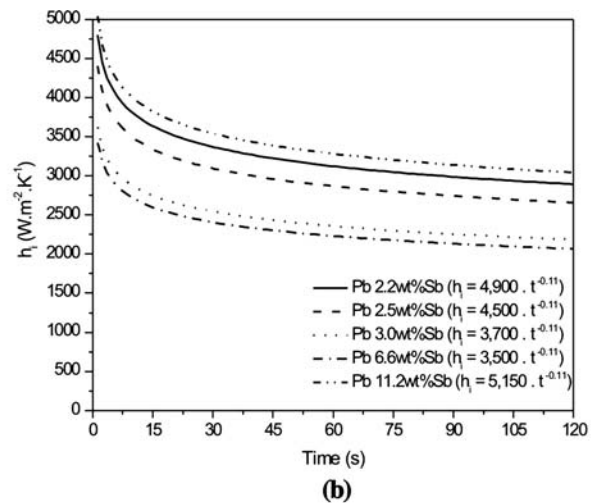
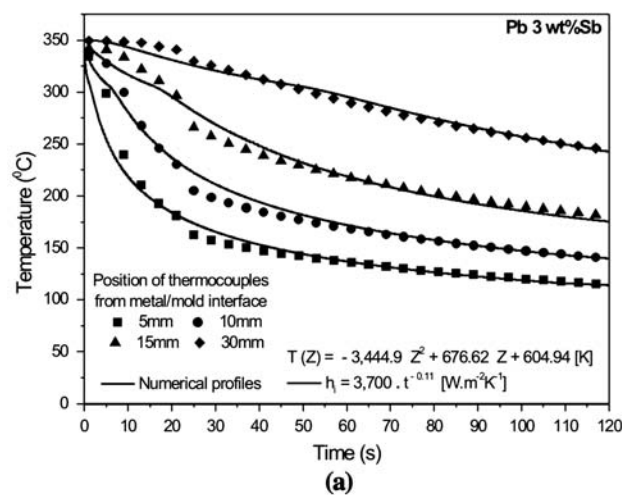


Fig. 3—(a) Best fit between simulated and experimental cooling curves that derived the transient h_i profile for a Pb-3 wt pct Sb alloy. (b) Comparison of the resultant experimental h_i profiles as a function of time for the Pb-Sb alloys experimentally examined. (c) Evolution of the multiplier A as a function of alloy Sb content. (d) Fluidity behavior of Pb-Sb alloys.

temperature gradient ahead of tip interface, and cooling rate, all of which vary with time and position. Thus, a numerical model is used to simulate the solidification of binary alloys in the cylindrical cavity chilled from the bottom. Initially, the alloys were assumed to be molten, quiescent, and uniformly mixed with a temperature T_p exceeding the liquidus temperatures. Melt convection and solid transport are both considered. The top and side walls were assumed to be insulated, while energy was extracted from the bottom at a rate governed by the overall metal-coolant heat-transfer coefficient h_i . The mathematical formulation of this solidification problem is based on that proposed previously by Voller.^[35] Some modifications have been incorporated into the original numerical approach, such as different thermophysical properties for the liquid and solid phases, transient metal/coolant heat-transfer coefficient, and a variable space grid to assure the accuracy of results without raising the number of nodes when comparing with experimental data, since a time-variable metal/mold interface heat-transfer coefficient will introduce a nonlinearity condition at the $z = 0$ boundary condition (Figure 4).

The vertical upward unidirectional solidification of a binary alloy is our target problem. This solidification takes place in an insulated cylindrical vertical mold cooled at the bottom. At time $t < 0$, the alloy is at molten state, at the nominal uniform concentration C_0 , and contained in the insulated mold defined by $0 < z < z_b$ (Figure 4). The initial melt temperature T_0 (at $t = 0$) is considered to vary with position in casting and is described by a parabolic function: $T_0(z) = az^2 + bz + c$. Solidification begins by cooling the metal at the chill ($z = 0$) until the temperature drops below the eutectic temperature T_{eut} . At times $t > 0$, three transient regions are formed: solid, solid + liquid (mushy zone), and

liquid. During this process, solute is rejected into the mushy zone.

In developing the numerical solution, the following assumptions were considered for equations of thermal and solute coupled fields.

- (1) The domain is one-dimensional, defined by $0 < z < z_b$, where z_b is a point far removed from the chill.
- (2) The solid phase is stationary, *i.e.*, once formed has zero velocity.
- (3) Due to the relatively rapid nature of heat and liquid mass diffusion, in a representative elemental averaging volume, the liquid concentration C_L , the temperature T , the liquid density ρ_L , and the liquid velocity u_L are assumed to be constants.^[35]
- (4) In the phase diagram, the partition coefficient k_0 and the liquid slope m are assumed to be constants.
- (5) Equilibrium conditions exist at the solid/liquid interface, *i.e.*, the temperature and concentrations fulfill the equation

$$T = T_f - mC_L \quad [12]$$

where T is the temperature, m is the slope of the liquidus line, C_L is the liquid concentration, and T_f is the fusion temperature of the pure solvent. The interface solid concentration, C_S^* , is related to C_L by the equilibrium partition coefficient, k_0

$$C_S^* = k_0 C_L \quad [13]$$

- (6) The specific heats c_s and c_L , thermal conductivities K_S and K_L , and densities ρ_S and ρ_L are constants within each phase, but discontinuous in the mushy zone (M), *i.e.*, $c_M = (1 - g_s) c_L + g_s c_s$, $K_M = (1 - g_s) K_L + g_s K_s$, and $\rho_M = (1 - g_s) \rho_L + g_s \rho_s$, where g_s is the local solid volume fraction. The latent heat of fusion ΔH is taken as the difference between phase enthalpies.
- (7) The metal/mold thermal resistance varies with time and is incorporated in a global heat-transfer coefficient defined as h_i .

The Thermo-Calc* software can be used to generate

*Thermo-Calc software is an exclusive copyright property of the STT Foundation (Foundation of Computational Thermodynamics, Stockholm).

equilibrium diagrams, and through the Thermo-Calc interface with MSDEV** COMPAQ VISUAL FORTRAN[†]

**MSDEV C is a trademark of Microsoft Corporation.

[†]COMPAQ VISUAL FORTRAN is a trademark of Compaq Computer Corporation.

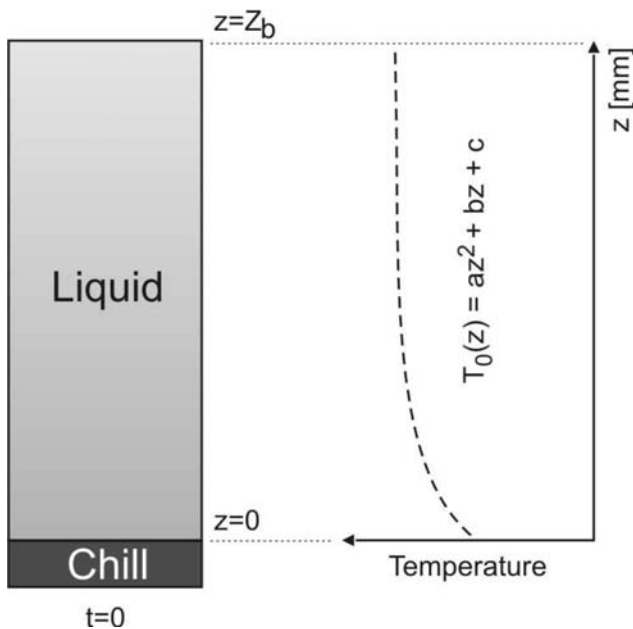


Fig. 4—Schematic initial melt temperature distribution for upward solidification ($t = 0$).

and Microsoft Visual C,** it is possible to recall those data generated by the software in order to provide more accurate results. In that way, Voller's scheme^[35] can be easily extended to deal with nonlinear behavior in the phase diagram.

Using the previously described assumptions, the mixture equations for binary solidification read as follows:

Energy:

$$\frac{\partial \rho c T}{\partial t} + \nabla \cdot (\rho_L c_L u T) = \nabla \cdot (K \nabla T) - \rho_S \Delta H \frac{\partial g}{\partial T} \quad [14]$$

Species:

$$\frac{\partial \rho C}{\partial t} + \nabla \cdot (\rho_L u C_L) = 0 \quad [15]$$

Mass:

$$\frac{\partial \rho}{\partial t} + \nabla \cdot (\rho_L u) = 0 \quad [16]$$

where g is the liquid volume fraction and u is the volume averaged fluid velocity defined as

$$u = g u_L \quad [17]$$

Mixture density:

$$\rho = \int_0^{1-g} \rho_S dx + g \rho_L \quad [18]$$

Mixture solute density:

$$\rho C = \int_0^{1-g} \rho_S C_S dx + g \rho_L C_L \quad [19]$$

where ρC is the volumetric specific heat, taken as volume fraction weighted averages. The boundary conditions at the domain are prescribed as

$$u = 0, \quad K \frac{\partial T}{\partial z} = h_i (T_0 - T|_{z=0}),$$

$$\text{and} \quad \frac{\partial C_L}{\partial z} = 0 \quad \text{at} \quad z = 0 \quad [20]$$

$$T \rightarrow T_p \text{ and } C_L \rightarrow C_0 \quad \text{at} \quad z = z_b \quad [21]$$

The numerical model, with the appropriate experimentally determined profile of transient heat-transfer coefficient, was used to calculate the solidification thermal variables commonly associated with the cellular and dendritic growth.

Figure 5 shows the experimentally determined cooling rate along the casting. It can be observed that a considerable range of cooling rate values was generated

as a result of the high heat extraction efficiency imposed by the water-cooled system, especially at the first stages of solidification. Furthermore, Figure 5 shows the simulated numerical profiles and it can be seen that good agreement is obtained between theory and experiments.

Figure 6 shows the liquidus isotherm velocity as a function of position for Pb-Sb alloys. After validating the numerical model against the experimental results, the calculated solidification thermal variables could be correlated to the cellular or dendritic spacing at any position from the casting surface.

Figure 7 shows the resultant directional solidified macrostructures obtained for Pb 2.2 wt pct Sb and 3.0 wt pct Sb alloy castings. For any alloy experimentally examined, the growth of columnar grains prevailed along the entire casting length.

Figure 8 shows typical microstructures of transverse (tr) and longitudinal (lg) sections of Pb 2.2, 2.5, and 6.6 wt pct Sb alloy castings. The cellular/dendritic transition (cdt) occurred during the unidirectional growth of the Pb 2.2 wt pct Sb alloy casting, with lateral perturbations appearing along a cooling rate range between 5.8 and 1.5 K/s. A completely dendritic pattern has been observed along the Pb 2.5, 3.0, and 6.6 wt pct Sb alloys castings, which included well-defined side perturbations typical of secondary dendrite arms, as the solute was increased.

Figure 9 shows mean, minimum, and maximum values of cellular (λ_c) and primary dendritic spacing (λ_1) as a function of the liquidus isotherm velocity for the Pb 2.2 wt pct Sb alloy casting. As similarly observed by Rocha and co-authors^[36] in studies carried out with Sn-Pb and Al-Cu alloys directionally solidified under non-steady-state conditions, the experimental law is governed by a -1.1 exponent, which applies for both cellular and primary dendritic growth. Rosa and co-authors^[5] have recently found the same exponent for the cellular growth of dilute Pb-Sb alloys (0.3, 0.85, and 1.9 wt pct Sb alloys). Concerning the spacing measurements carried out along the Pb-2.2 wt pct Sb alloy casting, the experimental law for cellular growth is characterized by a multiplier of about 2 times lower than that found for the dendritic growth.

Figure 10 shows the influence of cooling rate on the cellular/dendritic transition. The microstructures referring to positions close to the metal/mold interface, *i.e.*, for higher cooling rates (30 and 5 mm, respectively) have a well-defined dendritic array. At a position about 50 mm from the cooled surface, the microstructure begins to reveal cellular/dendritic transition features, characterized by wavy perturbations on the cellular pattern. However, as the cooling rate is increased during the transition range, a tendency of increase on the spacing has been observed (Figure 10). As soon as the dendrite pattern is clearly defined, the primary spacing decreases with the increase on cooling rate reverting again the growth tendency.

Eshelman and co-authors^[37] verified a similar behavior along the evolution of cellular and primary dendrite arm spacings as a function of tip growth rate during the solidification of succinonitrile-acetone under

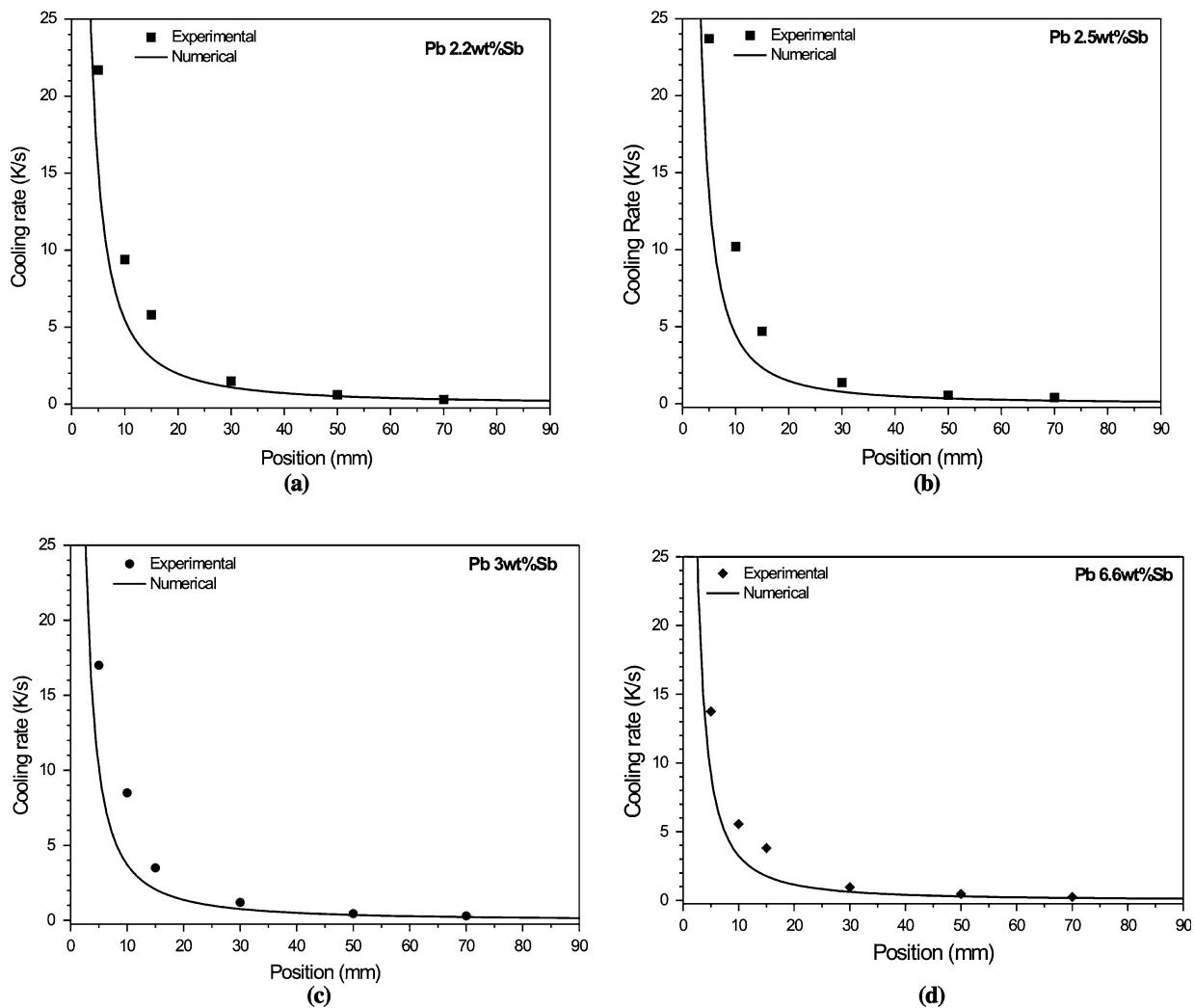


Fig. 5—Tip cooling rate as a function of position from the metal/mold interface during transient directional solidification of Pb-Sb alloys.

steady-state heat flow conditions. They also noted a significant increase in cellular spacings at the beginning of the transition range and have attributed such increase to an increase in amplitude of the cells. Rocha *et al.*^[19] have reported the same tendency during the investigation of cellular/dendritic transition of Sn-Pb alloys directionally solidified under non-steady-state conditions.

The examination of cellular and dendritic results as a function of cooling rate (Figure 10) reinforces the behavior observed in Figure 9. The -0.55 experimental power law was the same found in recent experimental studies on cellular and primary dendrite arm spacings of hypoeutectic Al-Cu,^[36] Sn-Pb,^[36,38] and Al-Si^[39,40] alloys.

The cooling rate dependences on primary dendritic spacings of Pb-2.5 wt pct Sb, Pb-3.0 wt pct Sb, and Pb-6.6 wt pct Sb alloys are shown in Figure 11, where average spacings along with the minimum/maximum range of experimental values are presented. The lines represent empirical power laws, which fit the experimental points. As observed for the Pb-2.2 wt pct Sb alloy, a -0.55 power law characterizes the primary dendrite arm spacing variation with cooling rate. It can

be seen in Figure 11 that the primary dendritic spacing seems to be independent of composition, since a single law has been sufficient to represent the variation of such spacing for the three hypoeutectic Pb-Sb alloys experimentally examined. Spittle and Lloyd^[41] have reported that both primary and secondary dendrite arm spacings of hypoeutectic Pb-Sb alloys solidified under steady and nonsteady freezing conditions decreased as the initial alloy composition increased. However, these authors have also reported that when the temperature gradient (G_L) was about $20\text{ }^\circ\text{C/mm}$, the spacings were independent of composition.

Rosa and collaborators^[5] have recently investigated the cellular growth of Pb-0.3 wt pct Sb, Pb-0.85 wt pct Sb, and Pb-1.9 wt pct Sb alloys during solidification under non-steady-state heat flow conditions. They found that a -0.55 power law also characterizes the cellular spacing variation with cooling rate. By comparing the experimental power laws obtained for dendritic growth of Pb-2.5 wt pct Sb, Pb-3.0 wt pct Sb, and Pb-6.6 wt pct Sb alloys and those obtained by Rosa *et al.*^[5] for cellular growth of Pb-Sb dilute alloys, it is

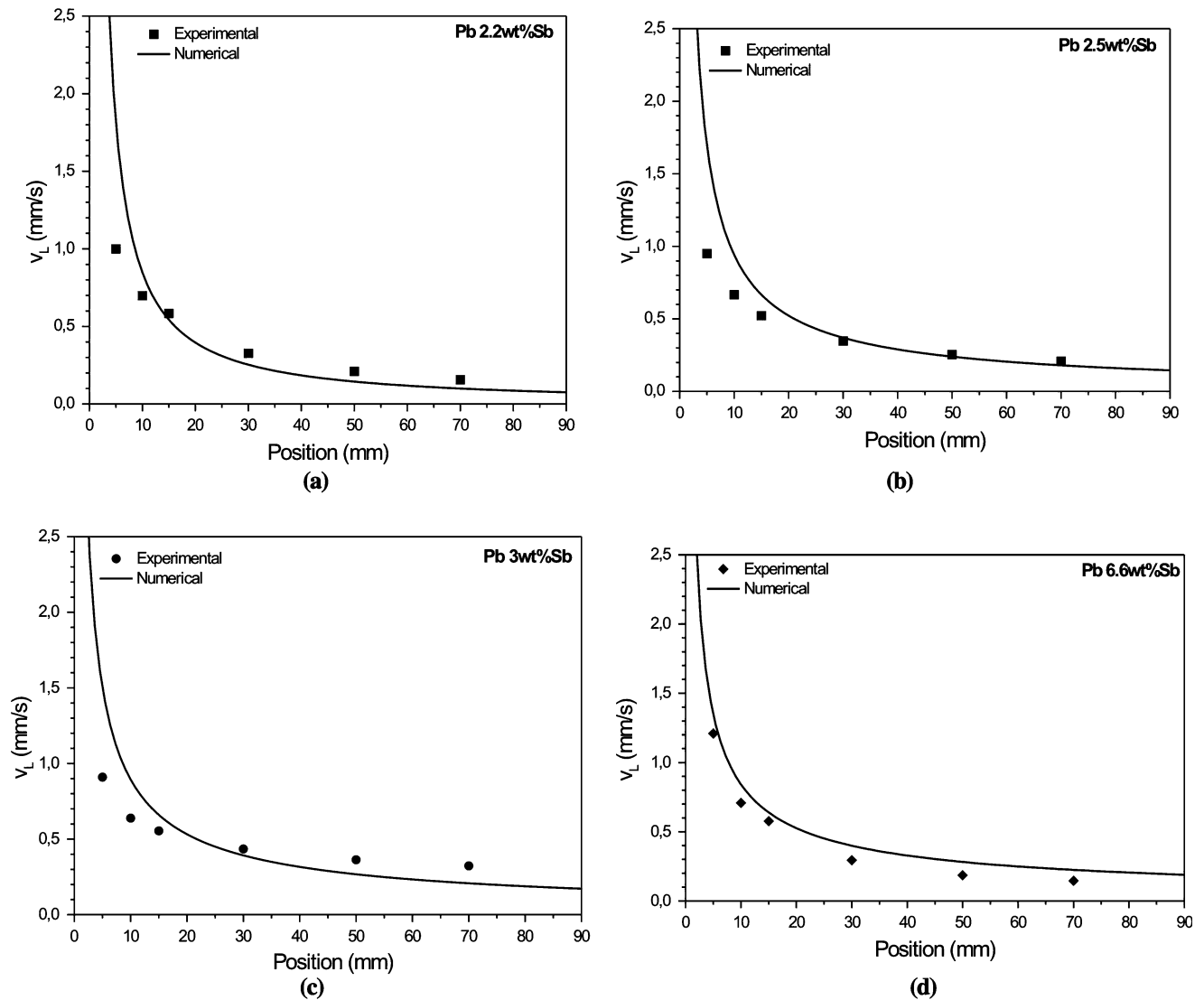


Fig. 6—Liquidus isotherm velocity as a function of position from the metal/mold interface.

possible to note that the multiplier ($A = \lambda_c \cdot \dot{T}^{0.55}$) is about 2 times lower than that found for the dendritic pattern observed in the present investigation. The points shown in Figure 12 represent the experimental A values obtained for each aforementioned alloy inside the cellular and dendritic growth regimes. It can be seen that $A = 60$ represent the alloys undergoing a cellular growth and $A = 115$ can describe the dendritic growth. The sudden change on the multiplier has occurred for the Pb 2.2 wt pct Sb alloy, *i.e.*, for the cellular/dendritic transition.

Lee *et al.*^[18] analyzed dendrite and cell spacings as a function of solidification velocity during steady-state directional solidification of stainless steels and have also reported that the dendrite spacings are larger than cellular spacings for a given velocity. Their experiments have also shown that the dendrite branch is at a higher spacing than the cellular branch for both low- and high-velocity cellular regimes.

Figure 13 shows the mean experimental values of secondary dendrite arm spacings (λ_2) as a function of liquidus isotherm velocity. As in Figure 11, points are experimental results and lines represent an empirical fit of the experimental points, with λ_2 being expressed as a power function of the velocity.

In order to analyze how the main steady-state theoretical predictive primary dendritic models perform against experimental results of nonsteady solidification, a comparison is made in Figure 14. It can be seen in general that, for any composition examined, the experimental scatter lies close to the calculations performed with Trivedi's model while Kurz-Fisher's model and Hunt's model overestimate and underestimate the experimental tendency, respectively.

Figure 15 shows comparisons between the present experimental results of primary spacings with theoretical predictions furnished by non-steady-state predictive models. They are the Hunt-Lu (HL) model represented

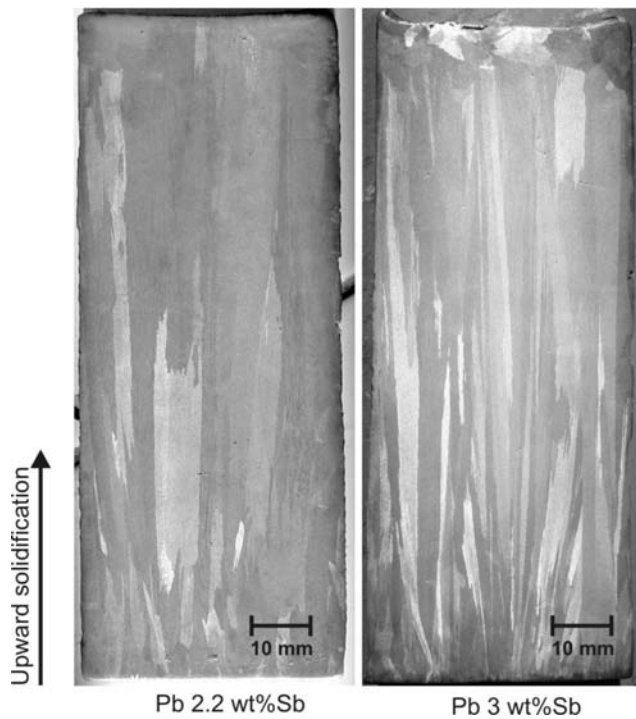


Fig. 7—Typical directionally solidified macrostructures.

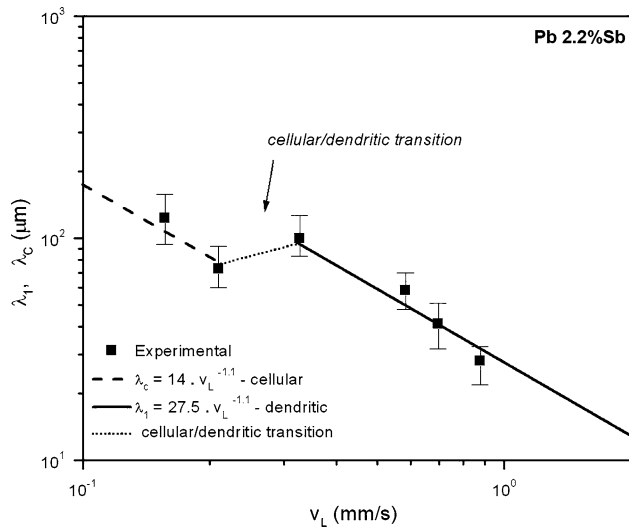


Fig. 9—Cellular (λ_c) and dendritic (λ_d) primary spacings as a function of liquidus isotherm velocity (V_L) for Pb 2.2 wt pct Sb alloy.

by Eqs. [4] and [5], and Bouchard–Kirkaldy (BK) model given by Eq. [7] with a calibration factor a_1 of 12 for Pb-Sb alloys, as suggested by these authors.^[13] The theoretical curve of the BK model accurately generated

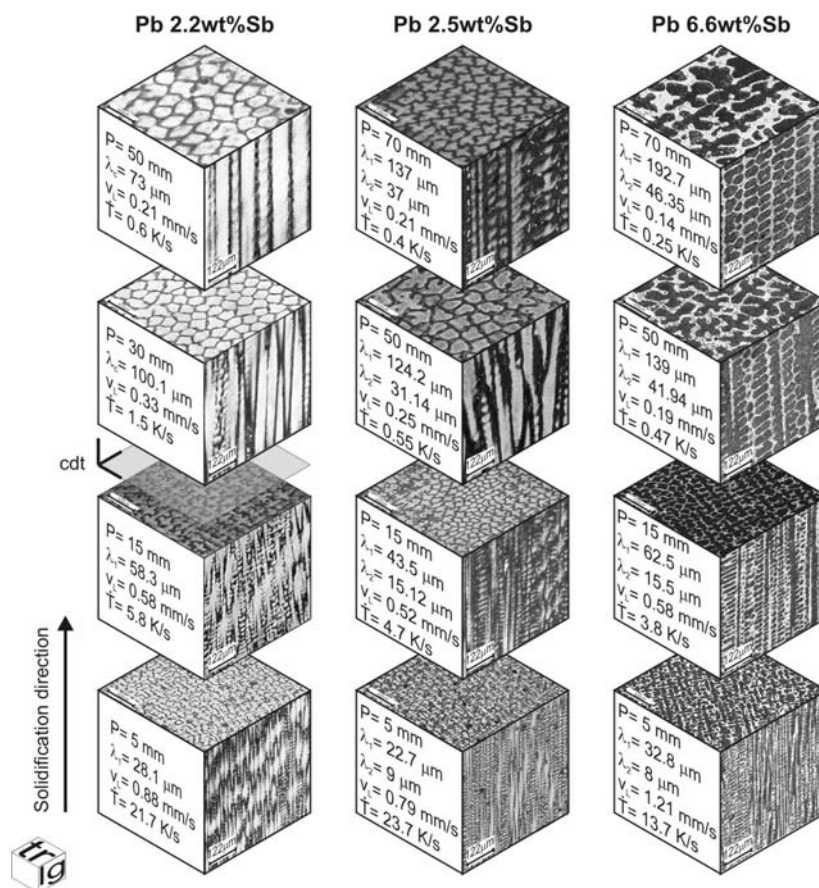


Fig. 8—Typical solidification microstructures along transverse (tr) and longitudinal sections (lg) of Pb 2.2, 2.5, and 6.6 wt pct Sb alloy castings (cdt is the end of cellular/dendritic transition range).

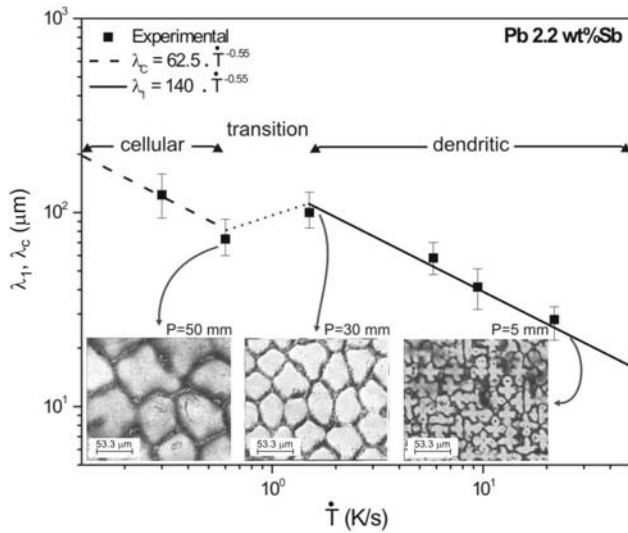


Fig. 10—Cellular (λ_c) and dendritic (λ_1) spacings as a function of tip cooling rate (\dot{T}) for a Pb 2.2 wt pct Sb alloy.

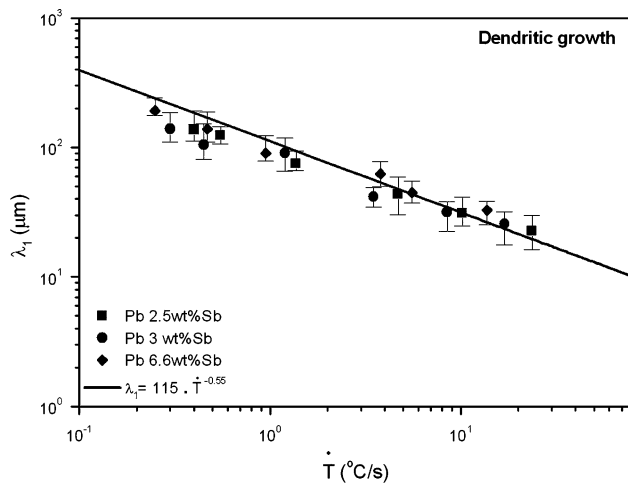


Fig. 11—Primary dendrite arm spacings as a function of cooling rate for Pb-Sb alloys.

the experimental observations, including the slope. The experimental points are located outside the maximum and minimum range of values predicted by the HL model, although very close to the curve of theoretical minimum spacings. The HL model has also been recently checked against other nonsteady solidification results, such as Sn-Pb^[36] and Al-Si alloys,^[40] and the theoretical predictions matched the experimental observations.

Hunt and Lu stated that problems might be expected to occur with the correlation of their model with experiment when extensive convection occurs. For hypoeutectic Pb-Sb alloys, the rejection of solute into the melt during upward vertical solidification results in reduced melt density, which causes convection in the mushy zone and immediately ahead of the cellular/dendritic array. A number of experimental studies have

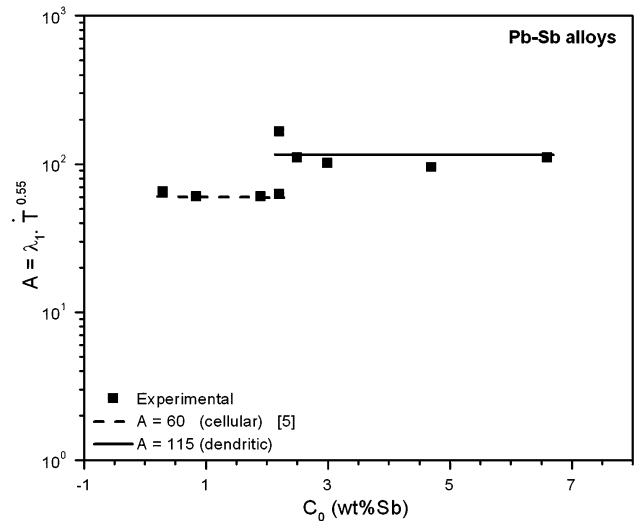


Fig. 12—Multipliers of the experimental growth laws as a function of Sb solute content.

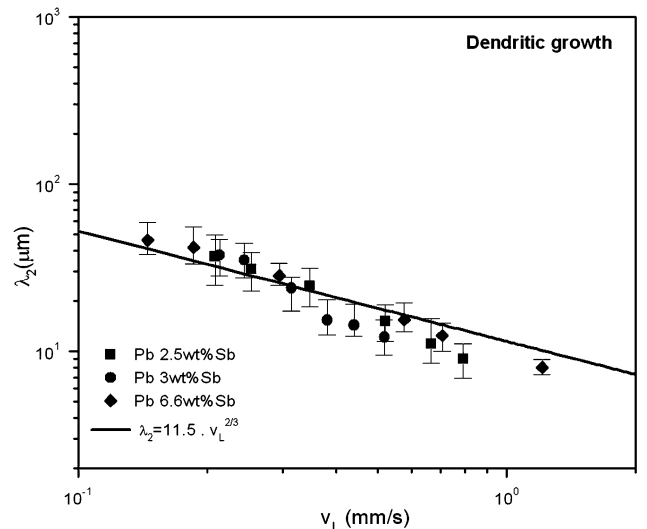


Fig. 13—Secondary dendrite arm spacing as a function of liquidus isotherm velocity for Pb-Sb alloys.

demonstrated the existence of a direct correlation between the decrease in the mean primary dendritic spacing and thermosolutal convection in the melt.^[38,40,42] Because convection is expected to influence the composition gradient in the melt, the dendritic spacings are also expected to be influenced by convection. Rosa *et al.*^[5] recently discussed theoretical cellular growth models and observed that dilute Pb-Sb alloys had not induced significant melt convection with the experimental cellular spacing scatter located above the theoretical predictions of the HL model. However, with higher Sb contents being tested in the present investigation, the influence of melt convection seems to occur, which resulted in experimental results only close to the HL model minimum values.

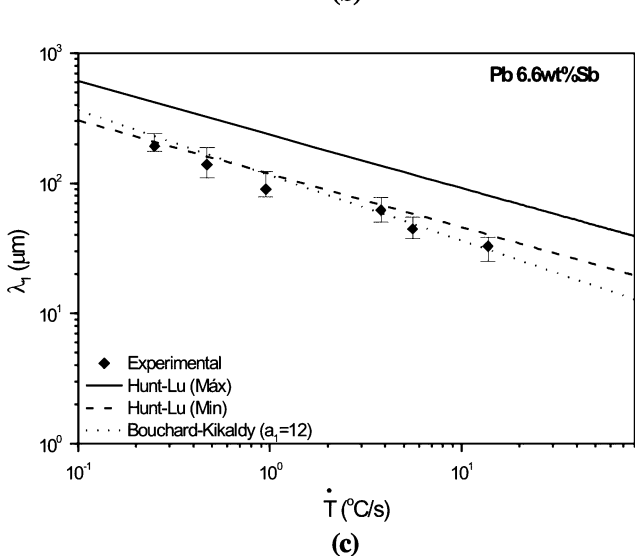
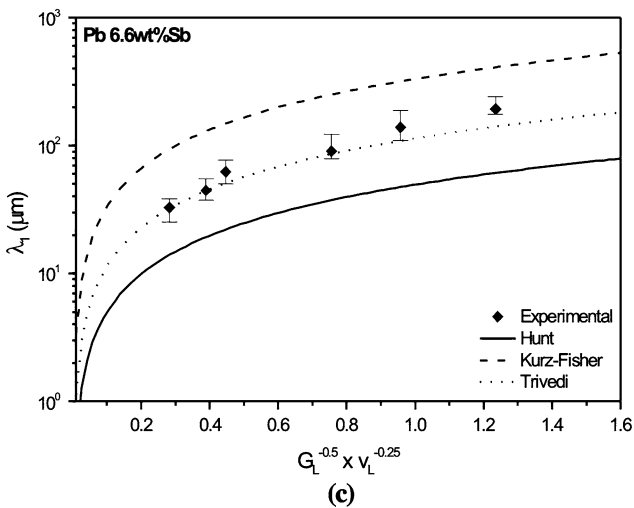
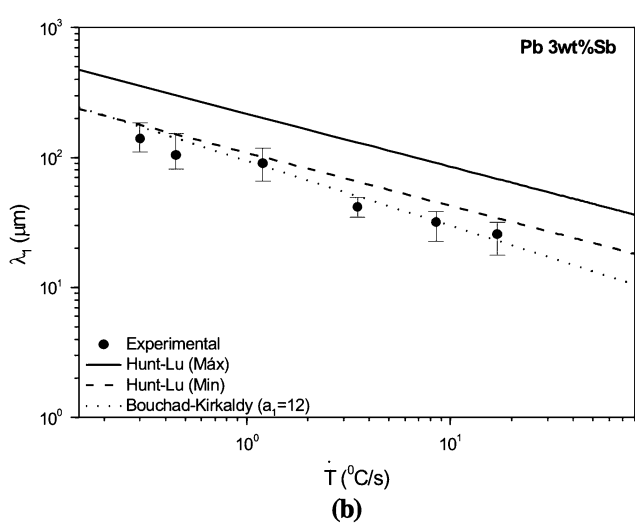
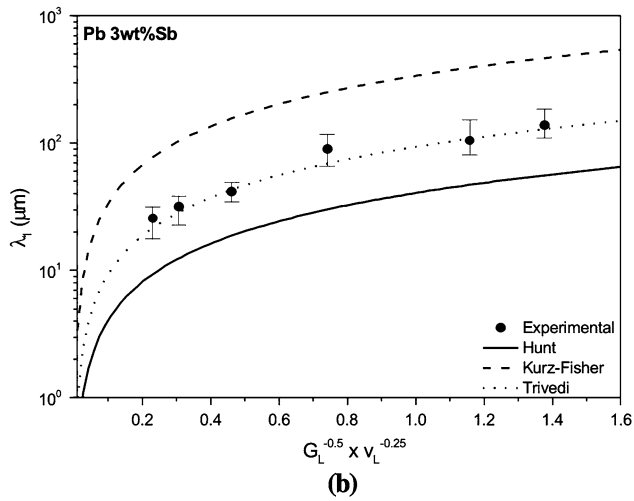
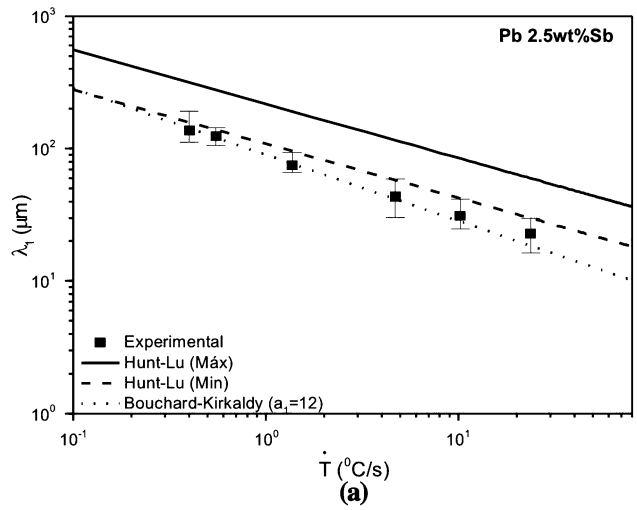
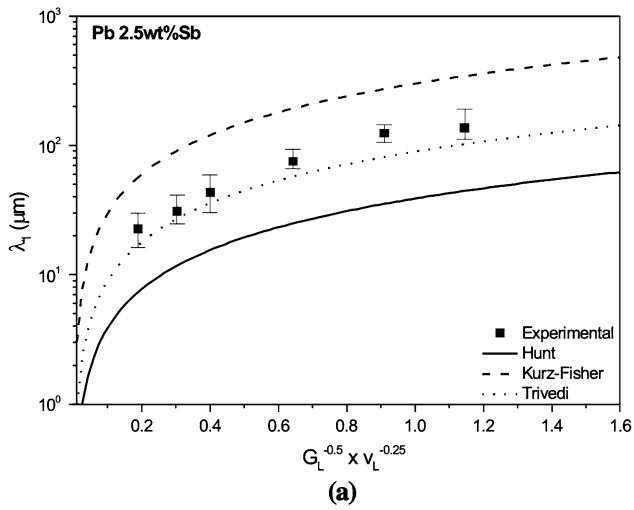


Fig. 14—Comparison of experimental (non-steady-state) and theoretical (steady-state) primary dendrite arm spacing for Pb-Sb alloys.

Figure 16 shows comparisons between the present experimental results of secondary dendrite arm spacings and theoretical predictions furnished by the BK model, given by Eq. [8] with a calibration factor a_2 of 2.65 for

Fig. 15—Comparison of experimental and theoretical primary dendrite arm spacing as a function of cooling rate for Pb-Sb alloys in non-steady-state directional solidification.

Pb-Sb alloys, as suggested by these authors.^[13] As can be seen, such model fits the experimental scatter for any alloy experimentally examined. Figure 16 also shows the

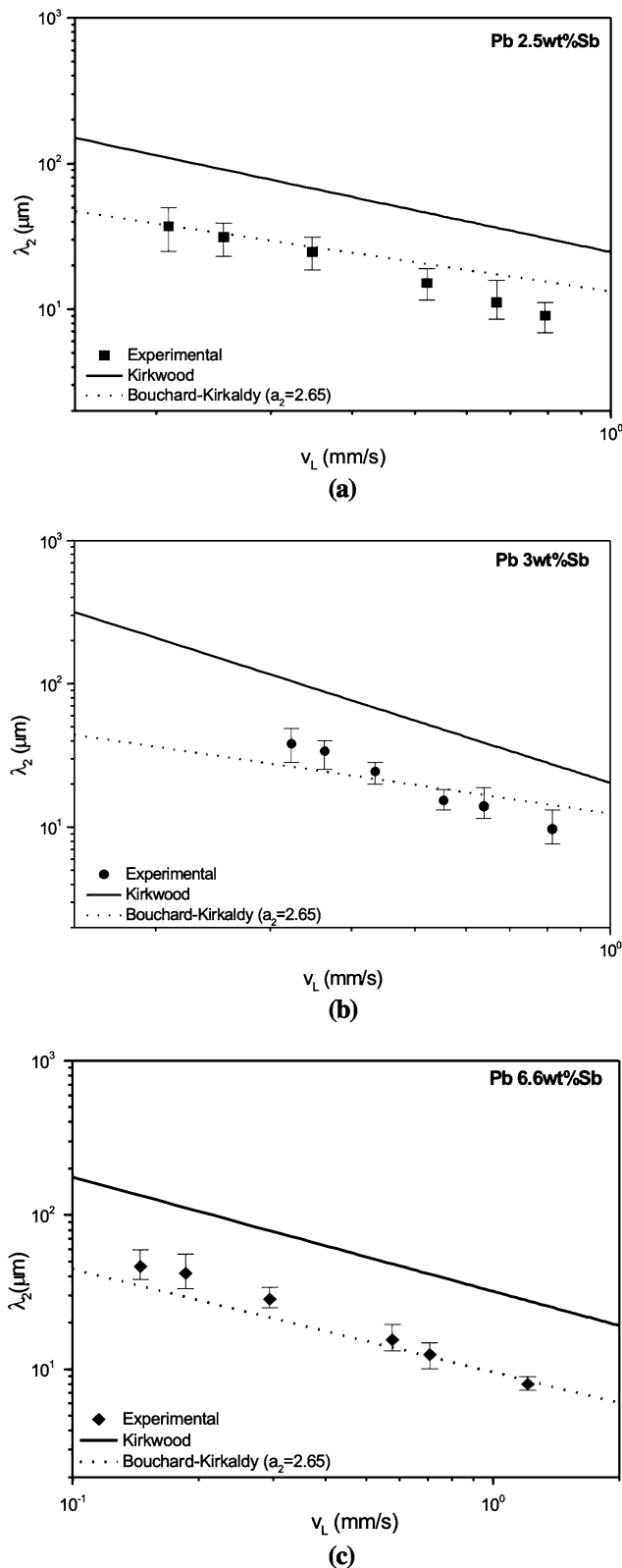


Fig. 16—Comparison of experimental and theoretical secondary dendrite arm spacing as a function of tip growth rate for Pb-Sb alloys.

predictions of Kirkwood model represented by Eq. [9]. It can be seen that the predictions of such model overestimate the experimental results.

V. CONCLUSIONS

The following main conclusions can be drawn from the present study.

1. A single exponent (0.11) has been found for the power laws characterizing the variation of the overall metal/coolant heat-transfer coefficient with time for hypoeutectic Pb-Sb alloys under the applied experimental conditions. In contrast, different multipliers have been obtained, which seem to be mainly linked to the wettability of the liquid layer in contact with the mold inner surface, *i.e.*, they have shown a behavior similar to that of the fluidity of such alloys.
2. An experimental law of the form $\lambda = A \cdot \dot{T}^{-0.55}$, which seems to be independent of composition, characterizes the cooling rate dependence on cellular and primary dendritic spacing, where $A = 60$ represents the alloys undergoing a cellular growth and $A = 115$ can describe the dendritic growth. The sudden change on the multiplier has occurred for the Pb 2.2 wt pct Sb alloy, *i.e.*, for the cellular/dendritic transition.
3. The experimental secondary dendritic arm spacing variation with the liquidus isotherm velocity has been characterized by a $-2/3$ experimental power law, and can be described by a single relationship for hypoeutectic Pb-Sb alloys.
4. The BK model theoretical curve accurately generated the experimental observations of primary dendritic arm spacing (λ_1) including the slope. In contrast, the λ_1 experimental scatter is located outside the maximum and minimum range of values predicted by the HL model, although very close to the curve of theoretical minimum spacings. Such behavior seems to be associated with thermosolutal convection in the melt. The rejection of Sb into the melt during upward vertical solidification results in reduced melt density, which causes convection in the mushy zone and immediately ahead of the dendritic array. The theoretical predictions for λ_2 furnished by the BK growth model properly match the experimental scatter.

ACKNOWLEDGMENTS

The authors acknowledge financial support provided by FAPESP (The Scientific Research Foundation of the State of São Paulo, Brazil), CNPq (The Brazilian Research Council), and FAEPEX -UNICAMP.

REFERENCES

1. L. Yu, G.L. Ding, J. Reye, S.N. Ojha, and S.N. Tewari: *Metall. Mater. Trans. A*, 1999, vol. 30A, pp. 2463–71.
2. S.P. O'Dell, G.L. Ding, and S.N. Tewari: *Metall. Mater. Trans. A*, 1999, vol. 30A, pp. 2159–65.
3. J. Hui, R. Tiwari, X. Wu, S.N. Tewari, and R. Trivedi: *Metall. Mater. Trans. A*, 2002, vol. 33A, pp. 3499–3510.

4. J. Chen, S.N. Tewari, G. Magadi, and H.C. de Groh, III: *Metall. Mater. Trans. A*, 2003, vol. 34A, pp. 2985–90.
5. D.M. Rosa, J.E. Spinelli, I.L. Ferreira, and A. Garcia: *J. Alloys Compd.*, 2006, vol. 422, pp. 227–38.
6. Y.E. Kalay, L.S. Chumbley, I.E. Anderson, and R.E. Napolitano: *Metall. Mater. Trans. A*, 2007, vol. 38A, pp. 1452–57.
7. S. Lu and S. Liu: *Metall. Mater. Trans. A*, 2007, vol. 38A, pp. 1378–87.
8. P.R. Goulart, J.E. Spinelli, W.R. Osório, and A. Garcia: *Mater. Sci. Eng. A*, 2006, vol. 421, pp. 245–53.
9. G.A. Santos, C. Moura Neto, W.R. Osório, and A. Garcia: *Mater. Des.*, 2007, vol. 28, pp. 2425–30.
10. W.R. Osório, P.R. Goulart, G.A. Santos, C. Moura Neto, and A. Garcia: *Metall. Mater. Trans. A*, 2006, vol. 37A, pp. 2525–38.
11. W.R. Osório, J.E. Spinelli, I.L. Ferreira, and A. Garcia: *Electrochim. Acta*, 2007, vol. 52, pp. 3265–73.
12. W.R. Osório, J.E. Spinelli, A.P. Boeira, C.M. Freire, and A. Garcia: *Microsc. Res. Technol.*, 2007, vol. 70, pp. 928–37.
13. D.M. Rosa, J.E. Spinelli, W.R. Osório, and A. Garcia: *J. Power Sources*, 2006, vol. 162, pp. 696–705.
14. W.R. Osório, D.M. Rosa, and A. Garcia: *J. Power Sources*, 2008, vol. 175, pp. 595–603.
15. G. Ding, W.D. Huang, X. Huang, X. Lin, and Y. Zhou: *Acta Mater.*, 1996, vol. 44, pp. 3705–09.
16. G. Ding, W.D. Huang, X. Lin, and Y. Zhou: *J. Cryst. Growth*, 1997, vol. 177, pp. 281–88.
17. J.D. Hunt: *Sci. Technol. Adv. Mater.*, 2001, vol. 2, pp. 147–55.
18. J.H. Lee, H.C. Kim, C.Y. Jo, S.K. Kim, J.H. Shin, S. Liu, and R. Trivedi: *Mater. Sci. Eng. A*, 2005, vols. 413–414, pp. 306–11.
19. O.L. Rocha, C.A. Siqueira, and A. Garcia: *Mater. Sci. Eng. A*, 2003, vol. 347, pp. 59–69.
20. R.D. Prengaman: *J. Power Sources*, 1997, vol. 67, pp. 267–78.
21. T. Hirasawa, K. Sasaki, M. Taguchi, and H. Kaneko: *J. Power Sources*, 2000, vol. 85, pp. 44–48.
22. J.D. Hunt and S.Z. Lu: *Metall. Mater. Trans. A*, 1996, vol. 27A, pp. 611–23.
23. D. Bouchard and J.S. Kirkaldy: *Metall. Mater. Trans. B*, 1997, vol. 28B, pp. 651–63.
24. Y.X. Zhuang, X.M. Zhang, L.H. Zhu, and Z.Q. Hu: *Sci. Technol. Adv. Mater.*, 2001, vol. 2, pp. 37–39.
25. W. Kurz and J.D. Fisher: *Acta Metall.*, 1981, vol. 29, pp. 11–20.
26. W. Kurz and J.D. Fisher: *Fundamentals of Solidification*, Trans Tech Publications, Aedermannsdorf, Switzerland, 1992, pp. 85–90.
27. R. Trivedi: *Metall. Mater. Trans. A*, 1984, vol. 15A, pp. 977–82.
28. U. Feurer and R. Wunderlin: cited by W. Kurz and D.J. Fisher: *Fundamentals of Solidification*, Trans Tech Publications Ltd., Aedermannsdorf, Switzerland, 1986, Appendix 8, pp. 214–16.
29. D.H. Kirkwood: *Mater. Sci. Eng. A*, 1985, vol. 73, pp. L1–L4.
30. M. Gunduz, H. Kaya, E. Çardili, N. Marasli, K. Keslioglu, and B. Saatçi: *J. Alloys Compd.*, 2007, vol. 439, pp. 114–27.
31. J.E. Spinelli, I.L. Ferreira, and A. Garcia: *Struct. Multidisc. Optim.*, 2006, vol. 31, pp. 241–48.
32. I.L. Ferreira, J.E. Spinelli, J.C. Pires, and A. Garcia: *Mater. Sci. Eng. A*, 2005, vol. 408, pp. 317–25.
33. N.F. Dewsnap and J. Devenport: *J. Inst. Met.*, 1967, vol. 95, pp. 263–67.
34. R.W. Heine, C.R. Loper, and P.C. Rosenthal: *Principles of Metal Casting*, McGraw-Hill, New York, NY, 1967, pp. 200–04.
35. V.R. Voller: *Can. Metall. Q.*, 1998, vol. 37, pp. 169–77.
36. O.L. Rocha, C.A. Siqueira, and A. Garcia: *Metall. Mater. Trans. A*, 2003, vol. 34A, pp. 995–1006.
37. M.A. Eshelman, V. Seetharaman, and J.W. Trivedi: *Acta Metall.*, 1998, vol. 36, pp. 1165–74.
38. J.E. Spinelli, I.L. Ferreira, and A. Garcia: *J. Alloys Compd.*, 2004, vol. 384, pp. 217–26.
39. M.D. Peres, C.A. Siqueira, and A. Garcia: *J. Alloys Compd.*, 2004, vol. 381, pp. 168–81.
40. J.E. Spinelli, M.D. Peres, and A. Garcia: *J. Alloys Compd.*, 2005, vol. 403, pp. 228–38.
41. J.A. Spittle and D.M. Lloyd: *Int. Conf. Solidification and Casting of Metals*, The Metals Society, London, 1979, pp. 15–20.
42. M.D. Dupouy, D. Camel, and J.J. Favier: *J. Cryst. Growth*, 1993, vol. 126, pp. 480–88.